

# MorphGS: Morphology-Adaptive Articulated 3D Motion Transfer from Videos

Taeyeon Kim\* Youngju Na\* Jumin Lee Sebin Lee Minhyuk Sung Sung-eui Yoon†

*Department of Computer Science, KAIST*

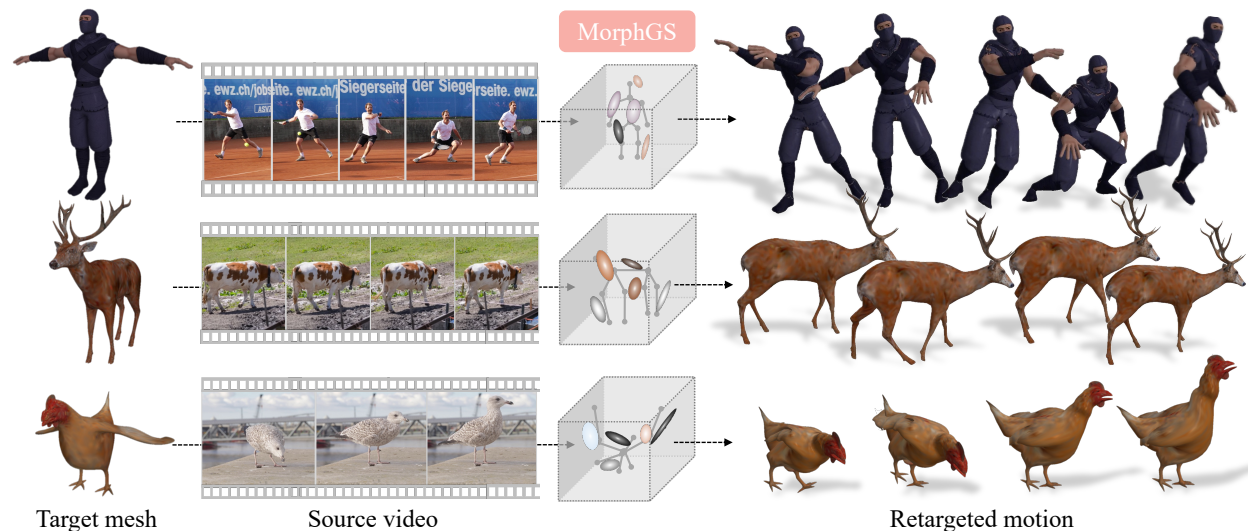


Figure 1: Given a monocular video and a rigged 3D target character, MorphGS directly optimizes target morphology and pose parameters to reproduce the observed motion without explicit source 3D reconstruction or category-specific parametric templates.

## Abstract

Transferring articulated motion from monocular videos to rigged 3D characters is challenging due to pose ambiguity in 2D observations and morphological differences between source and target. Existing approaches often follow a reconstruct-then-retarget paradigm, tying transfer quality to intermediate 3D reconstruction and limiting applicability to categories with parametric templates. We propose MorphGS, a framework that formulates motion retargeting as a target-driven analysis-by-synthesis problem, directly optimizing target morphology and pose through image-space supervision. A rig-coupled morphology parameterization factorizes character identity from time-varying joint rotations, while dense 2D-3D correspondences and synthesized views provide complementary structural and multi-view guidance. Experiments on synthetic benchmarks and in-the-wild videos show consistent improvements over baselines.

## 1 Introduction

Animating 3D characters from videos has long been a goal in vision and graphics. At its core, the task requires retargeting articulated motion observed in a monocular video to a rigged 3D target character. Despite progress in video-based 3D motion reconstruction, robust motion retargeting from monocular videos remains challenging to deploy broadly, as source videos and target characters often differ substantially in morphology and appearance [49, 2].

\*Equal contribution †Corresponding author

A common paradigm follows a *reconstruct-then-retarget* pipeline [10, 30, 66, 51, 32]: first reconstruct an intermediate 3D representation from the source video, then transfer the recovered motion to a target character. These approaches often rely on parametric templates [28, 72], category-specific models [56, 16, 61], or large-scale training data [24], limiting their applicability to well-studied categories such as humans and quadrupeds. Furthermore, the cascaded nature of the pipeline causes errors to propagate into the retargeting stage, where they are further amplified by morphological mismatches between the source and target.

We propose **MorphGS**, a video-to-3D motion transfer framework (Fig. 1) that casts retargeting as a *target-driven analysis-by-synthesis* problem [21, 6, 50]. Instead of reconstructing the source in 3D, we directly optimize the target character’s morphology and motion parameters so that its differentiable rendering [18] reproduces the source observations, while its structural identity remains anchored to the target.

The key to making this target-driven optimization tractable is to prevent pose updates from entangling with shape changes. MorphGS introduces an explicit morphology parameterization that factorizes time-invariant character identity from time-varying motion. Concretely, we model shape with structured morphology parameters—bone lengths, scale, and local rest-pose offsets anchored to the rig—while optimizing per-frame pose parameters via image-space supervision. To provide robust structural guidance, we incorporate dense 2D-3D semantic correspondences that supply part-level anchors, and leverage diffusion-based novel-view synthesis to generate multi-view pseudo-observations that provide complementary multi-view supervision.

We evaluate MorphGS on established synthetic benchmarks and in-the-wild real videos. Across both settings, MorphGS achieves robust performance across evaluated settings in motion fidelity and morphology preservation, without relying on category-specific templates or 3D supervision.

## 2 Related Work

Our study addresses video-to-3D motion transfer, where the goal is to recover a pose sequence that animates a rigged 3D target mesh to reproduce articulated motion observed in videos. This task builds upon 3D motion transfer and pose estimation from 2D. We review each area below along with existing 2D-to-3D motion transfer methods, and position our approach within this landscape.

**Pose and shape estimation from videos** Recovering 3D pose from video often relies on category-specific parametric templates such as SMPL [28] for humans [67, 13] and SMAL [72] for quadrupeds [39, 29]. These methods achieve strong results but remain confined to categories for which dense 3D annotations and parametric models exist. Template-free methods [61, 55, 56, 4, 24] predict 3D shape and pose from image collections without predefined templates, yet their category-specific training limits generalization beyond seen categories and does not extend to cross-character retargeting. Recent advances in 4D reconstruction have enabled per-scene articulated modeling from monocular or sparse observations, leveraging representations such as 3D Gaussian splatting [18, 15, 54, 14, 63] and mesh-Gaussian hybrids [23, 57]. Other approaches leverage automatic rigging or video diffusion priors to animate static meshes [43, 53]. However, these methods remain subject-specific, as the recovered motion is tied to the source identity and does not directly transfer to other characters.

**3D-to-3D motion transfer** While the above methods focus on recovering motion for the same subject, motion retargeting addresses transferring articulation across different characters. Classical approaches operate on explicit skeletal representations [12, 49, 2, 48, 8], yielding robust results when two characters share compatible rigs. Skeleton-free deformation methods [11, 52, 25, 51, 32, 65] relax the need for structural alignment but still require high-quality 3D motion sequences (*e.g.*, mesh animations or skeletal trajectories) as input, which remain scarce beyond well-studied categories such as humans.

**2D-to-3D motion transfer** Video-driven 3D motion transfer combines pose estimation and retargeting into a single pipeline. In the human and quadruped domains, parametric templates [28, 72] are paired with pose estimators [67, 38] and 3D transfer techniques [5, 51, 32] to form effective pipelines, but these remain inherently limited to categories that such templates support. Meanwhile, category-agnostic methods [30, 66, 10] extend this to arbitrary object categories. Transfer4D [30] estimates skeletal motion from RGB-D reconstructed meshes, requiring depth sensors. Other approaches [10, 66] remove this dependency through neural bone reconstruction [60] or image-to-3D generative models [27, 7], enabling template-free transfer across

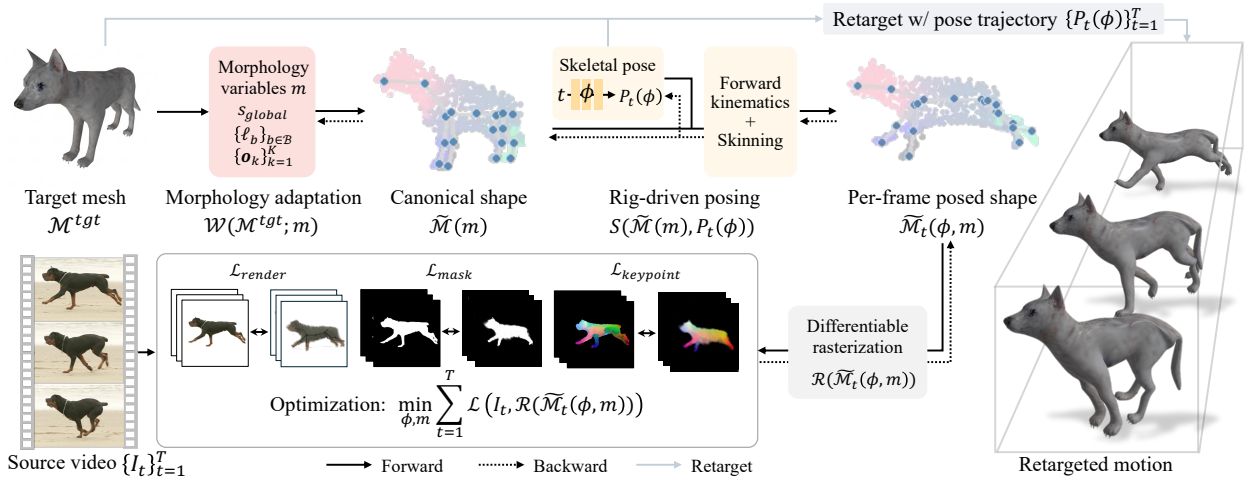


Figure 2: **Overview of MorphGS.** Given a source video and a target character, MorphGS first represents the target as morphology-adaptive articulated 3D mesh (Sec. 3.2). 3D Gaussian representation is wrapped to deform pose and render differentially (Sec. 3.3). The morphology and pose parameters are jointly optimized through image-space supervision (Sec. 3.4). The recovered motion is then retargeted to the target character, yielding an animation that closely follows the source video.

diverse categories. Despite their generality, these approaches follow a reconstruct-then-retarget paradigm in which motion is first extracted from the source and then transferred to the target, tying performance to the quality of the intermediate reconstruction.

In contrast, our method casts video-to-3D retargeting as a target-driven analysis-by-synthesis problem, directly optimizing the target’s morphology and pose through image-space supervision via differentiable Gaussian rendering. A skeletal-anchored morphology parameterization accounts for the shape differences between source and target while preserving the target’s rig, enabling transfer between morphologically different characters without parametric templates or explicit 3D supervision.

## 3 Methods

### 3.1 Problem Formulation

Consider a source monocular RGB video  $\{I_t \in \mathbb{R}^{H \times W \times 3}\}_{t=1}^T$  depicting an articulated subject. Given a rigged target mesh  $\mathcal{M}^{tgt}$  whose morphology may differ from the source, our goal is to estimate a temporally coherent pose trajectory  $\{P_t\}_{t=1}^T$  that retargets the observed motion onto  $\mathcal{M}^{tgt}$  while preserving the target’s structural identity (i.e., skeleton topology and mesh connectivity).

**Target-driven analysis-by-synthesis** We formulate video-to-3D motion retargeting as a target-driven analysis-by-synthesis problem. Instead of reconstructing the source in 3D and transferring motion afterward, we directly optimize target-specific parameters so that the rendering of the animated target closely reproduces the input frames. At each time step  $t$ , the posed shape  $\tilde{\mathcal{M}}_t$  is obtained in two stages: (i) *morphology adaptation* in the target’s canonical space, which adjusts limb proportions, global scale, and local geometry to bridge the shape gap between the source and target, followed by (ii) *rig-driven posing* via forward kinematics and linear blend skinning:

$$\tilde{\mathcal{M}}(m) = \mathcal{W}(\mathcal{M}^{tgt}; m), \quad \tilde{\mathcal{M}}_t(\phi, m) = \mathcal{S}(\tilde{\mathcal{M}}(m), P_t(\phi)), \quad (1)$$

where  $\mathcal{W}(\cdot; m)$  is the morphology adaptation function parameterized by  $m$ , producing the adjusted canonical shape  $\tilde{\mathcal{M}}$ , and  $\mathcal{S}$  denotes the skinning operator that applies skeletal pose  $P_t(\phi)$  to  $\tilde{\mathcal{M}}$ , yielding the per-frame posed shape  $\tilde{\mathcal{M}}_t$ . Here  $\phi$  denotes the parameters of a temporally conditioned pose network.

A differentiable renderer  $\mathcal{R}$  maps the posed shape  $\tilde{\mathcal{M}}_t$  to a predicted frame  $\hat{I}_t = \mathcal{R}(\tilde{\mathcal{M}}_t)$ , where we adopt the 3D Gaussian rasterizer [18] for efficient rendering. We estimate target-side parameters  $(\phi, m)$  by minimizing

objectives in the projection space over the foreground mask  $\Omega_t$ :

$$\min_{\phi, m} \sum_{t=1}^T \mathcal{L}(I_t, \mathcal{R}(\tilde{\mathcal{M}}_t(\phi, m)); \Omega_t). \quad (2)$$

By optimizing entirely in the target’s parameter space, this formulation bypasses intermediate 3D source reconstruction. Once optimization is complete, only the recovered pose trajectory  $\{P_t(\phi)\}_{t=1}^T$  is applied to the original target rig  $\mathcal{M}^{\text{tgt}}$ , preserving its original geometry. Note that we fix intrinsics and do not estimate per-frame extrinsics in our renderer. Global source–target alignment in each frame is approximated by a per-frame root transform in  $SE(3)$ .

Building on the above formulation, we first introduce a morphology-adaptive parameterization for articulated 3D modeling (Sec. 3.2), then describe pose-conditioned Gaussian rendering (Sec. 3.3), and finally present the full objective and optimization procedure (Sec. 3.4). Overall pipeline is illustrated in Fig. 2.

### 3.2 Morphology-Parameterized Articulated 3D Modeling

The goal of the morphology adaptation function  $\mathcal{W}$  is to account for time-invariant shape differences between the source subject and the target character (*e.g.*, differences in limb proportions, body size, or local geometry), so that the per-frame source observations can be explained primarily by the pose trajectory  $\{P_t(\phi)\}_{t=1}^T$  through the skinning operator  $\mathcal{S}$  (Eq. (1)).

However, jointly optimizing shape and pose from monocular observations is challenging due to the well-known shape-pose ambiguity, where shape changes can compensate for pose updates in the image plane [58, 17]. If the canonical shape is optimized without structural and temporal constraints, it can absorb per-frame pose errors and lead to geometric drift. We mitigate this by restricting all shape changes to structured *time-invariant* morphology parameters coupled to the target rig, thereby reducing the degrees of freedom that can explain the same 2D observations. Accordingly, we parameterize morphology as:

$$m = \left( s_{\text{global}}, \{\ell_b\}_{b \in \mathcal{B}}, \{\mathbf{o}_k\}_{k=1}^K \right), \quad (3)$$

where  $s_{\text{global}} \in \mathbb{R}_+$  resolves monocular depth–scale ambiguity,  $\ell_b \in \mathbb{R}_+$  are learnable bone lengths controlling skeletal proportions, and  $\mathbf{o}_k \in \mathbb{R}^3$  are local geometric offsets that capture residual shape details (*e.g.*, limb thickness, silhouette) beyond what the skeleton alone can express, as illustrated in Fig 3. We assume the target mesh  $\mathcal{M}^{\text{tgt}}$  is rigged with a fixed kinematic tree and skinning weights  $\{w_{kj}\}$ . For unrigged targets (*e.g.*, generated mesh), we obtain these using an off-the-shelf auto-rigging methods [5, 68].

**Learnable bone lengths** Let  $\mathcal{J}$  denote the set of joints with root joint  $j_{\text{root}}$ . For each bone  $b \in \mathcal{B}$ ,  $\mathbf{d}_b$  denotes the unit direction from its parent to child joint. We define the rest-pose joint locations  $\mathbf{j}_{\text{rest}} : \mathcal{J} \rightarrow \mathbb{R}^3$  as:

$$\mathbf{j}_{\text{rest}}(j; \ell) = \mathbf{j}_{\text{rest}}(j_{\text{root}}) + \sum_{b \in \mathcal{P}(j_{\text{root}}, j)} \ell_b \mathbf{d}_b, \quad (4)$$

where  $\mathcal{P}(j_{\text{root}}, j)$  denotes the kinematic-chain path (set of bones) from the root to joint  $j$ . The kinematic tree  $\mathcal{B}$  and unit directions  $\mathbf{d}_b$  are initialized from the target rig and kept fixed, while only the bone lengths  $\ell_b$  are optimized. This preserves the skeletal topology while allowing bone proportions to adapt via  $\ell_b$  for all  $b \in \mathcal{B}$ .

**Canonical target shape** Given the adjusted skeleton, we define each canonical vertex position relative to the rig. Specifically, we compute a skeleton-dependent anchor  $\mathbf{p}_k$  as the skinning-weighted average of the rest joints:

$$\mathbf{p}_k = \sum_{j \in \mathcal{J}} w_{kj} \mathbf{j}_{\text{rest}}(j; \ell). \quad (5)$$

With normalized skinning weights ( $w_{kj} \geq 0, \sum_j w_{kj} = 1$ ),  $\mathbf{p}_k$  is a convex combination of joint locations and therefore lies in the convex hull of  $\{\mathbf{j}_{\text{rest}}(j)\}$ . We then model the canonical vertex as a residual around this

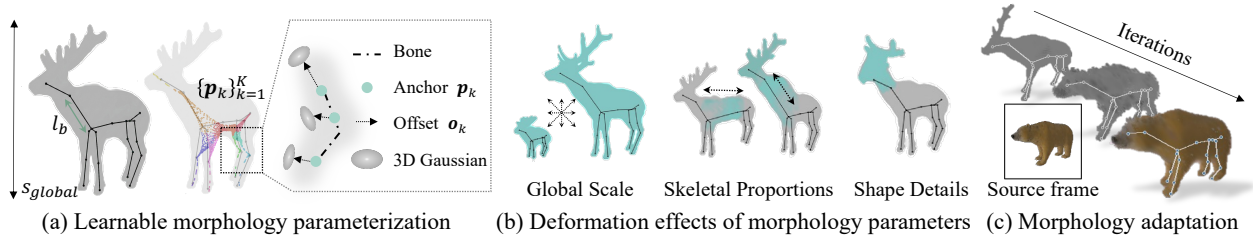


Figure 3: **Morphology parameterization.** (a) An overview of skeleton anchor  $\mathbf{p}_k$ , local offset  $\mathbf{o}_k$ , and 3D Gaussian primitives on the target rig. (b) Distinct motion deformation induced by global scale, bone lengths, and offset Gaussians. (c) An example of morphology adaptation.

anchor,  $\mathbf{v}_k = \mathbf{p}_k + \mathbf{o}_k$ , where  $\mathbf{o}_k \in \mathbb{R}^3$  is a skeletal anchored rest-space offset relative to  $\mathbf{p}_k$  that captures local residual geometry (*e.g.*, thickness, silhouette) beyond skeletal proportions.

Finally, we apply a uniform global scale  $s_{\text{global}} \in \mathbb{R}_+$  to the canonical shape, including both the skeleton and surface geometry, to resolve the monocular depth-scale ambiguity:

$$\bar{\mathbf{v}}_k = s_{\text{global}} \mathbf{v}_k. \quad (6)$$

**Discussion** Theoretically, recovering both 3D shape and motion from monocular 2D trajectories with unconstrained non-rigid structure is ill-posed [58]. Under weak-perspective projection, our formulation instead imposes a piecewise-rigid kinematic model in which bone lengths  $\{l_b\}$  and local rest-space offsets  $\{\mathbf{o}_k\}$  are strictly time-invariant [20]. This factorization confines temporal variation to articulated joint rotations, which discourages morphology parameters from compensating for pose errors and reduces shape–pose entanglement. With sufficiently non-degenerate motion, the resulting kinematic constraints make morphology and pose identifiable up to a global scale factor. While real videos often deviate from these ideal assumptions (*e.g.*, perspective effects and soft-tissue deformation), the analysis provides a useful explanation for the empirical stability of our target-driven optimization. We include a proof sketch and further discussion in the appendix.

### 3.3 Pose-conditioned Gaussian Rendering

Our target-driven formulation jointly optimizes both the morphology parameters  $m$  and the pose parameters  $\phi$  through image-space gradients. We realize this by representing the morphology-adapted canonical shape as an articulated 3D Gaussian set, posing it through forward kinematics and Linear Blend Skinning (LBS), and rendering via 3D Gaussian splatting [18].

**Articulated 3D Gaussians** We represent the target mesh with  $K$  3D Gaussian primitives, initialized from the mesh vertices in the rest pose so that each Gaussian inherits its vertex’s skinning weights  $\{w_{kj}\}_{j \in \mathcal{J}}$  directly from the rig. Each primitive  $k$  carries a canonical center  $\bar{\mathbf{v}}_k \in \mathbb{R}^3$  (Eq. 6) together with the standard splatting attributes: anisotropic scale, rotation vector, opacity, and view-dependent color [18]. This initialization ensures that skeletal deformations and surface geometry remain tightly coupled, preventing the Gaussians from drifting away from the underlying rig during optimization.

**Pose-conditioned deformation** To encourage temporal coherence, we parameterize the pose trajectory with a single time-conditioned network rather than optimizing independent per-frame pose:

$$P_t(\phi) = (\{\boldsymbol{\theta}_j^t\}_{j \in \mathcal{J}}, \boldsymbol{\delta}_{\text{root}}^t) = f_\phi(\text{emb}(t)), \quad (7)$$

where  $\text{emb}(t)$  is a sinusoidal time embedding [47, 31] and  $f_\phi$  is a lightweight MLP that outputs per-joint relative rotations  $\boldsymbol{\theta}_j^t$  (axis-angle) and root translation  $\boldsymbol{\delta}_{\text{root}}^t$ . Forward kinematics converts the local rotations into global joint transforms  $\{\mathbf{T}_j^t \in \text{SE}(3)\}_{j \in \mathcal{J}}$ , which then deform the canonical centers via LBS:

$$\mathbf{v}_k^t = \sum_{j \in \mathcal{J}} w_{kj} \mathbf{T}_j^t \bar{\mathbf{v}}_k. \quad (8)$$

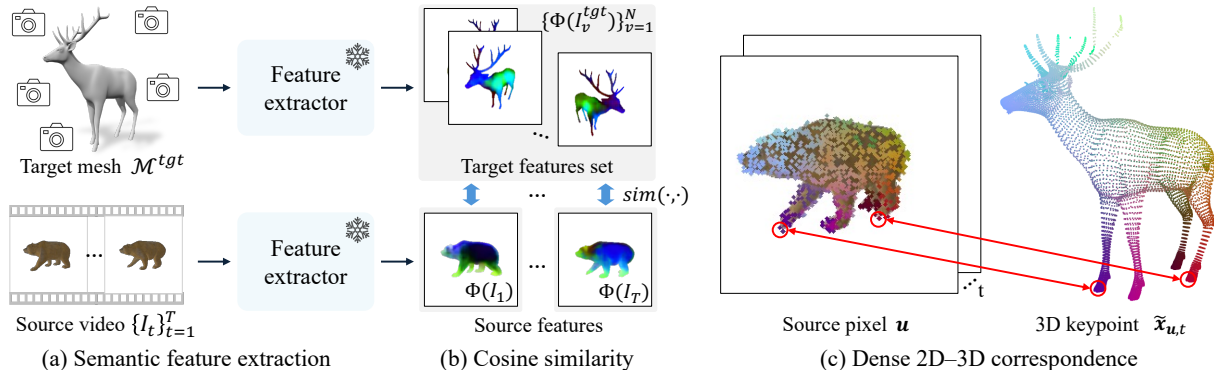


Figure 4: **Dense 2D-3D correspondences matching.** (a) Extracting semantic features from source frames and rendered target views. (b) Calculating similarity between them. (c) 3D keypoint mapping corresponding to the source pixel.

**Rasterization** The posed Gaussians are projected onto the image plane and composited via depth-sorted alpha blending [18], producing a rendered frame  $\hat{I}_t = \mathcal{R}(\mathcal{M}_t(\phi, m))$ . This closes the differentiable chain from  $(m, \phi)$  to the pixel-level objective in Eq. 2, enabling joint morphology–pose optimization through image-space supervision alone.

### 3.4 Differentiable Optimization Framework

During the optimization, the Gaussian representation serves as a differentiable proxy, enabling image-space gradients to flow back to both shape and pose through the rendering pipeline. Unlike prior pipelines that assume aligned source–target [63, 14, 40] or require canonical pose initialization [43], our approach jointly optimizes morphology and pose from an in-the-wild video without such assumptions. Our objective combines rendering losses, keypoint loss, and regularization:

$$\mathcal{L}_t = \underbrace{\mathcal{L}_{\text{rgb}} + \mathcal{L}_{\text{mask}}}_{\mathcal{L}_{\text{render}}} + \mathcal{L}_{\text{keyp}}. \quad (9)$$

**Rendering losses** The rendering terms provide the primary gradient signal for motion and appearance alignment by directly comparing the rendered target  $\hat{I}_t$  with the source frame  $I_t$  in the image plane. Specifically,  $\mathcal{L}_{\text{rgb}}$  enforces photometric consistency within the foreground region, and  $\mathcal{L}_{\text{mask}}$  aligns the rendered alpha mask  $\hat{\Omega}_t$  with a foreground segmentation  $\Omega_t$  to stabilize global outline.

**Keypoint loss** Photometric and mask supervision provide robust appearance and shape signals, but can be insufficient early in optimization or under large source–target morphological differences, where pixel-level losses alone struggle to establish reliable part-to-part correspondences. To provide explicit structural guidance, we establish dense 2D–3D correspondences between the source frame and the target mesh and use them as keypoint supervision.

*Dense 2D–3D correspondence.* The detailed pipeline of our dense correspondence extraction module is illustrated in Fig 4. We first extract dense semantic features from the source video frames  $\{I_t\}_{t=1}^T$  and from the rendered images of the target mesh across  $N$  views,  $\{I_v^{\text{tgt}}\}_{v=1}^N$ , using a geometry-aware feature extractor  $\Phi(\cdot)$  [69]. For each frame  $t$ , we define  $\mathbf{u} \in \mathbb{R}^2$  as a foreground pixel in the source frame  $I_t$ , and  $\mathbf{x} \in \mathbb{R}^3$  as a vertex from the target mesh vertices  $\mathcal{V}(\mathcal{M}^{\text{tgt}})$ . Following SHIC [41], we compute the pooled similarity score between  $\mathbf{u}$  and  $\mathbf{x}$ :

$$\Sigma_t(\mathbf{u}, \mathbf{x}) = \text{pool}_{v, \mathbf{x} \in \mathcal{V}(\mathcal{M}^{\text{tgt}})} \text{sim}(\Phi(I_t)[\mathbf{u}], \Phi(I_v^{\text{tgt}})[\pi_v(\mathbf{x})]), \quad (10)$$

where  $\text{sim}(\cdot, \cdot)$  denotes cosine similarity,  $\pi_v(\mathbf{x})$  projects  $\mathbf{x}$  onto rendered view  $I_v^{\text{tgt}}$ , and pool operator aggregates scores across all  $N$  rendered views. Each source pixel is then assigned to its best-matching 3D keypoint  $\tilde{\mathbf{x}}_{\mathbf{u},t}$ :

$$\tilde{\mathbf{x}}_{\mathbf{u},t} = \arg \max_{\mathbf{x} \in \mathcal{V}(\mathcal{M}^{\text{tgt}})} \Sigma_t(\mathbf{u}, \mathbf{x}). \quad (11)$$

*Keypoint supervision.* Let  $\mathcal{P}_t$  denote the set of sampled foreground pixels in frame  $t$ . For each frame  $t$ , we select source pixels  $\mathbf{u}_i \in \mathcal{P}_t$ , whose similarity scores exceed a confidence threshold, and penalize the reprojection error between their observed locations and the projected positions of the matched 3D keypoints:

$$\mathcal{L}_{\text{keyp}} = \frac{1}{\sum_t |\mathcal{P}_t|} \sum_t \sum_{\mathbf{u}_i \in \mathcal{P}_t} \rho(\mathbf{u}_i - \pi(\tilde{\mathbf{x}}_{\mathbf{u}_i, t})), \quad (12)$$

where  $\pi(\cdot)$  denotes a fixed camera projection, and  $\rho(\cdot)$  is a smooth- $\ell_1$  penalty.

**Synthesized-view guidance** Monocular input leaves occluded body parts under-constrained, making pose ambiguous under self-occlusion. To provide complementary viewpoints, we leverage a diffusion-based novel-view synthesis module [62] to generate temporally consistent pseudo-views of the source sequence. Our target-driven formulation naturally accommodates multi-view supervision, as the synthesized views simply provide additional image-space objectives over the same target parameters. We extend the rendering losses to all viewpoints  $\mathcal{C}$ :

$$\mathcal{L}_{\text{mv}} = \sum_{t=1}^T \sum_{c \in \mathcal{C}} \mathcal{L}_{\text{render}, t}^{(c)}. \quad (13)$$

This additional supervision regularizes pose estimation under self-occlusion, where the monocular input alone provides insufficient constraints.

**Regularizations** Finally,  $\mathcal{L}_{\text{reg}}$  enforces frame-to-frame temporal motion smoothness. Additional details on regularizations are provided in the Appendix.

## 4 Experiments

### 4.1 Implementation details

We employ a staged optimization strategy that first resolves global alignment (root translation, root orientation,  $s_{\text{global}}$ ), then we enable updating  $\ell_b$ , and local joint rotation estimation from 500 to 1.5K iterations. Lastly, from 1.5K iterations, we jointly optimize all parameters, including Gaussian splatting attributes (offsets  $\mathbf{o}_k$ , color, scale, rotation). All experiments are run on a single NVIDIA RTX 4090 GPU. For a target mesh with 10K vertices, the optimization process takes approximately 5 minutes for 5K iterations using Adam [19] with adaptive learning rates. Further details are provided in the appendix.

### 4.2 Experimental Setup

**Datasets** We evaluate MorphGS on both real-world and synthetic benchmarks to assess motion transfer performance across different categories. For synthetic evaluation, we test on Mixamo [3] and DeformingThings-4D (DT4D) [22], following prior motion-transfer protocols [25, 65].

In the Mixamo dataset, we utilize 12 humanoid source–target pairs with different motion types including diverse human motions (*e.g.*, jumping, running, and dancing), where rigged target meshes are directly available from the dataset. For DT4D, we include 20 animal source–target pairs with paired posed mesh sequences for the same motion, split into two groups by skeleton topology: *DT4D-Quadrupeds* (four-legged animals), and *DT4D-Others*, which includes 5 categories beyond the standard quadruped skeleton topology. Since DT4D does not provide rigged meshes, we obtain target rigs using off-the-shelf auto-rigging tools [5, 68]. To generate source videos, we animate the target with the ground-truth pose sequence and render a monocular video from a fixed viewpoint using the differentiable mesh renderer in PyTorch3D [36], yielding 1,505 pairs of source–target mesh in total across the three splits.

For real-world evaluation, we curate 8 object-centric clips covering both human and animal motions from DAVIS [34] and publicly available stock videos on Pexels [1], together with a small set of generated clips. These scenes span diverse capture conditions and motion complexities, from dynamic human actions to in-the-wild animal motion, as illustrated in Fig. 1 and Fig. 6.

Table 1: **Quantitative evaluation on Mixamo and DT4D datasets.** Our method consistently outperforms all baselines across evaluated datasets on average. Results are averaged across scenes, with per-scene results in the appendix. PMD ( $\times 10^3$ ,  $\downarrow$ ) measures geometric accuracy and FVMD ( $\times 10^{-3}$ ,  $\downarrow$ ) measures perceptual motion fidelity.

Method	Mixamo-Humanoids		DT4D-Quadrupeds		DT4D-Others	
	PMD	FVMD	PMD	FVMD	PMD	FVMD
SPT <sup>+</sup>	2.96	12.56	–	–	–	–
NPR <sup>+</sup>	3.98	16.67	3.28	16.32	–	–
Transfer4D	7.65	16.16	4.67	15.34	7.16	17.52
Pinocchio <sup>+</sup>	4.55	14.03	5.56	15.24	7.59	14.23
Ours	<b>1.91</b>	<b>8.82</b>	<b>1.33</b>	<b>8.81</b>	<b>2.90</b>	<b>12.85</b>

Table 2: **Quantitative evaluation on real-world videos.** We use FVMD ( $\times 10^{-3}$ ,  $\downarrow$ ) as the quantitative metric for motion fidelity.

Method	Human scenes					Animal scenes				
	tennis	ballet	hockey	snowboard	avg	bear	camel	cows	dog	avg
SPT <sup>+</sup>	13.95	5.40	5.53	19.30	11.05	–	–	–	–	–
NPR <sup>+</sup>	21.03	11.41	11.96	19.81	18.48	29.54	17.46	14.62	25.85	19.05
Pinocchio <sup>+</sup>	16.91	<b>4.45</b>	7.64	18.38	11.85	18.27	13.80	12.58	24.33	17.24
Ours	<b>13.87</b>	5.39	<b>5.13</b>	<b>18.07</b>	<b>10.61</b>	<b>13.31</b>	<b>12.28</b>	<b>6.43</b>	<b>21.15</b>	<b>13.29</b>

**Evaluation metrics** For synthetic datasets, we measure Point-wise Mesh Distance (PMD) [71, 52] across all frames to evaluate motion transfer accuracy as the average per-vertex  $\ell_2$  distance between the retargeted and ground-truth meshes following [25, 51, 65]. For both synthetic and real datasets, we measure Fréchet Video Motion Distance (FVMD) [26], which measures perceptual motion plausibility by comparing distributions of velocity and acceleration features extracted from keypoint trajectories in rendered videos.

**Baselines** We compare against baselines from two groups. (i) The first follows a *reconstruct-then-retarget* paradigm, where a 3D mesh sequence is first reconstructed from the source RGB video using off-the-shelf parametric template pose estimators [13, 29], and then retargeted to the target character via SPT [25] (denoted SPT<sup>+</sup>), NPR [65] (denoted NPR<sup>+</sup>), or Pinocchio [5] (denoted Pinocchio<sup>+</sup>). (ii) The second is Transfer4D [30], which estimates a motion skeleton from RGB-D input and transfers it to the target via automatic rigging.

### 4.3 Motion Transfer Comparisons

We evaluate motion transfer on synthetic benchmarks spanning humanoid characters and animal targets with different topologies. Tab. 1 summarizes the results across categories.

**Humanoid motion transfer** For reconstruct-then-retarget baselines, we first estimate SMPL [28] pose sequences from the source video using an off-the-shelf monocular human pose estimator [13], and then retarget the recovered 3D motion to the target character using SPT [25], NPR [65], and Pinocchio [5], respectively. For Transfer4D [30], which requires RGB-D input, we additionally provide rendered metric depth maps.

As shown in the first column of Tab. 1, MorphGS shows lower PMD and FVMD than the compared baselines, consistent with the qualitative results in Fig. 5. Baseline methods often exhibit incomplete motion transfer (*e.g.*, third row of Fig. 5) or over-smoothed deformations. This is because they rely on learned pose priors or latent manifold constraints, and retargeting stage may prioritize globally plausible motion over fine-grained vertex-level alignment. In addition, preprocessing targets into manifold mesh representations [25, 65] can remove high-frequency surface details. MorphGS instead optimizes target morphology and pose via

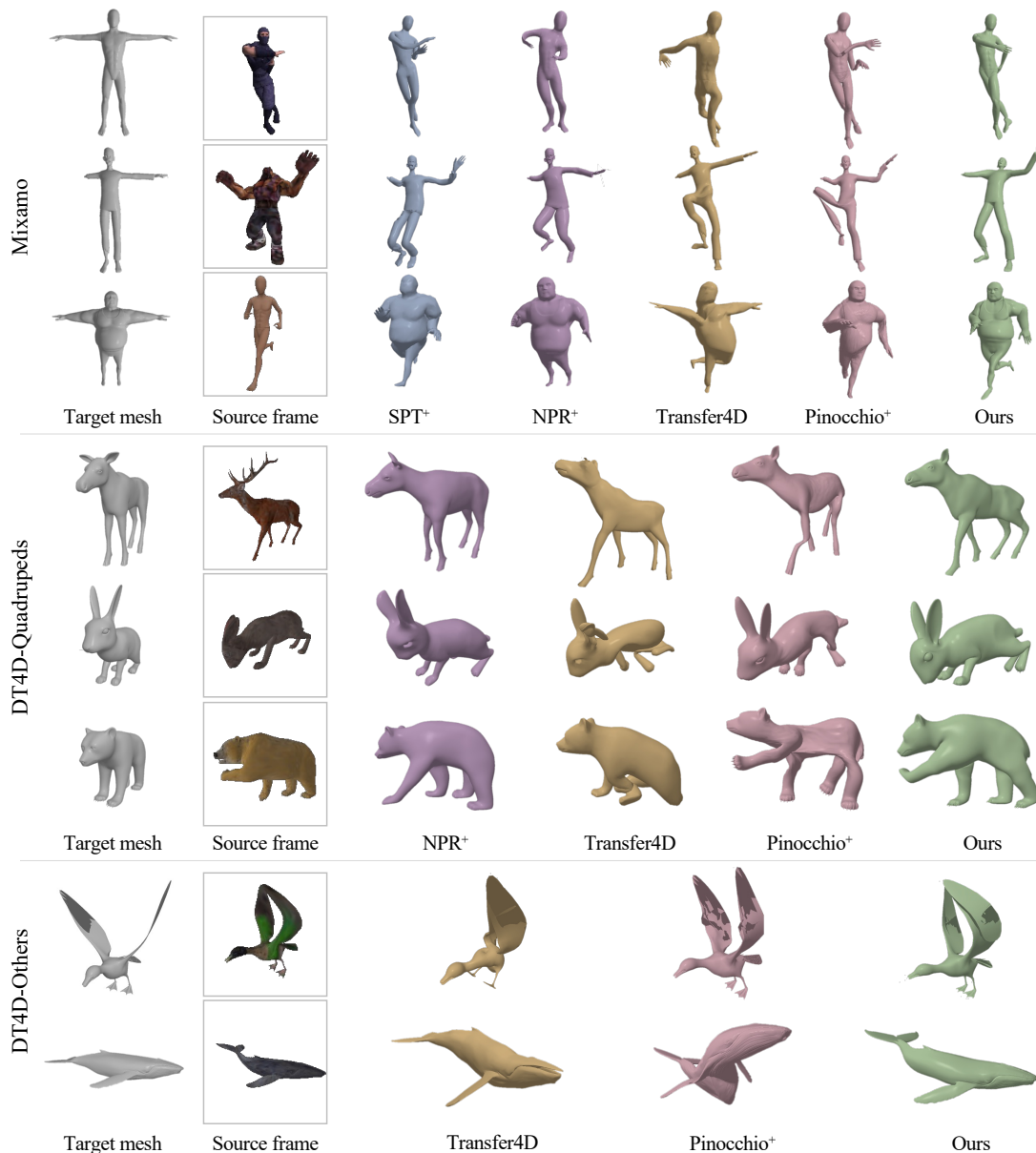


Figure 5: **Qualitative results on Mixamo and DT4D datasets.** Our method shows superior pose alignment compared to baselines across diverse objects.

differentiable rendering in the target parameter space, which maintains target mesh structure while showing reasonable pose alignment to source motions as in Fig. 5.

**Animal motion transfer** We further report animal motion transfer results in the DT4D-Quadrupeds and DT4D-Others columns of Tab. 1. For reconstruct-and-retarget baselines, we use [29] to reconstruct SMAL [72] template pose sequences from the source videos. We omit SPT+ for animals because pretrained weights are not available for non-human shapes. NPR+ is omitted on DT4D-Others since it requires pretrained pose manifolds, which are not provided for non-quadruped animal categories.

For DT4D-Others, which includes categories beyond common parametric templates such as bird or whale, we compare our method against Transfer4D and Pinocchio+. For Pinocchio+ on these categories, we provide a ground-truth source mesh sequence as input, bypassing the 2D video-to-3D reconstruction stage to avoid severe error propagation from an intermediate reconstruction pipeline. As shown in Tab. 1, MorphGS shows

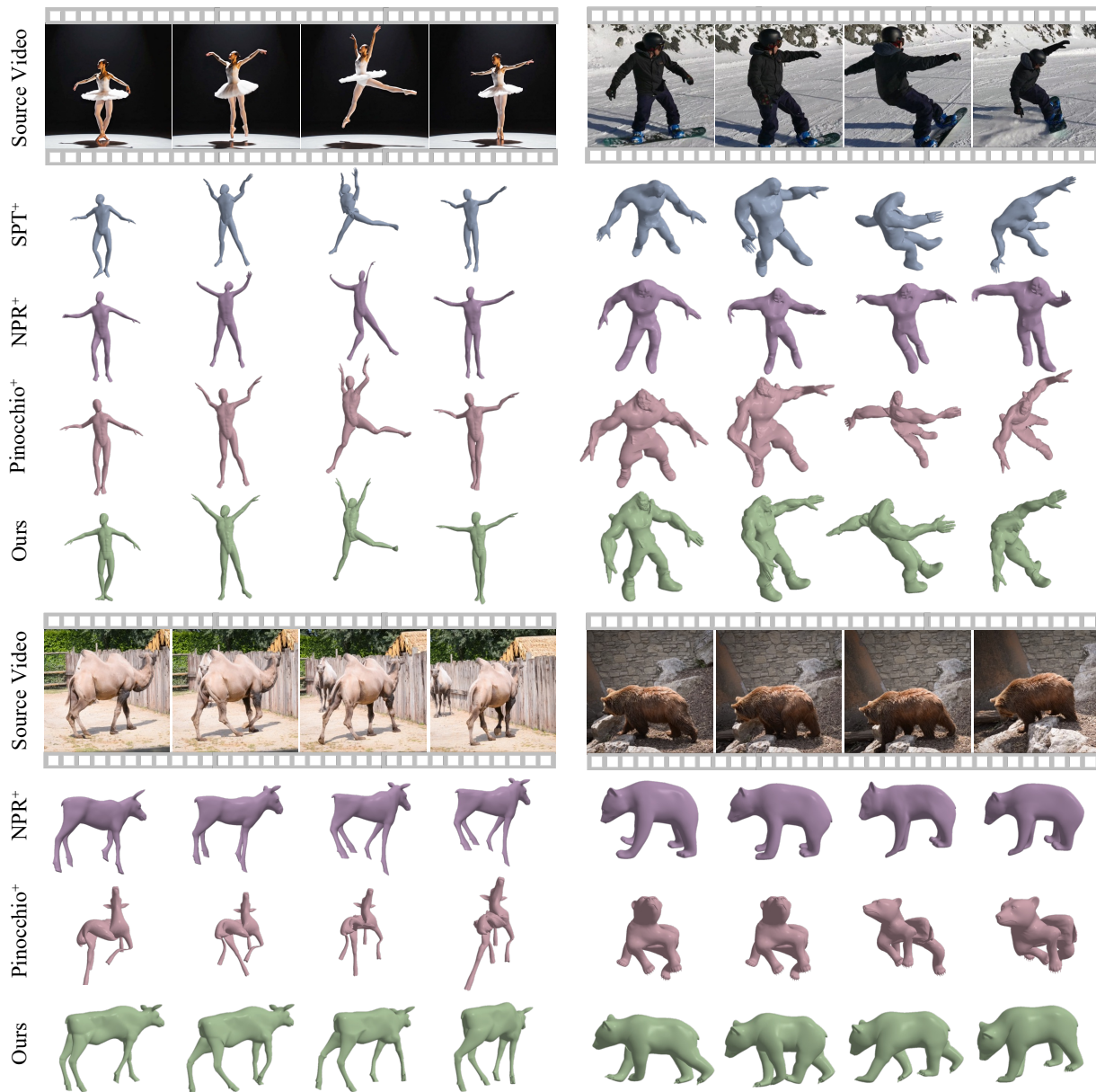


Figure 6: **Qualitative results on real-world videos.** We show motion transfer results on in-the-wild videos.

lower PMD and FVMD than both baselines, demonstrating reasonable motion transferring performance on non-standard categories that remain relatively underexplored in the motion retargeting literature.

**Real-world video-to-3D motion transfer** We evaluate on real-world monocular videos by using in-the-wild clips as motion sources. Since ground-truth 3D mesh sequences are unavailable for such footage, we report FVMD [26] as a perceptual measure of motion consistency. We use target meshes from Mixamo [3] for humanoids and DT4D [22] for animals. As summarized in Tab. 2, MorphGS achieves a lower average FVMD than the compared baselines on both human and animal videos. Qualitative results in Fig. 6 show that the posed targets track the motion in the input frames while maintaining the target’s original structure. These results indicate that our target-driven, morphology-adaptive optimization is effective on unconstrained monocular videos [28, 72].

Table 3: **Ablation study.** PMD ( $\times 10^3$ ,  $\downarrow$ ) and FVMD ( $\times 10^{-3}$ ,  $\downarrow$ ) are averaged over 12 scenes from the Mixamo [3] dataset.

Model	PMD	FVMD
<i>Morphology parameterization</i>		
Naïve model	8.45	17.54
Fixed morphology	3.72	15.30
+ $\ell_b$	2.87	12.45
+ $\ell_b, s_{\text{global}}$	1.99	9.55
+ $\ell_b, s_{\text{global}}, \mathbf{o}_k$	1.91	8.82
<i>Supervision losses</i>		
$\mathcal{L}_{\text{render}}$	4.52	13.57
+ $\mathcal{L}_{\text{keyp}}$	2.96	11.93
+ $\mathcal{L}_{\text{keyp}}, \mathcal{L}_{\text{mv}}$	1.91	8.82

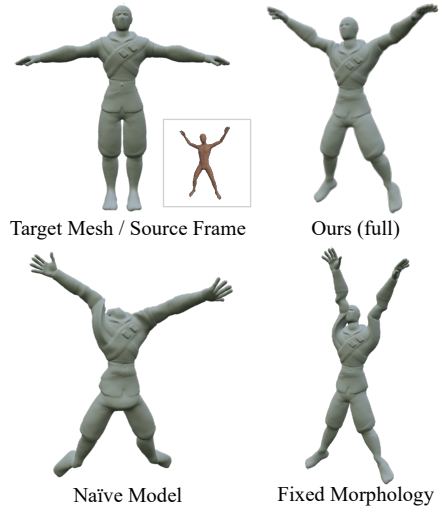


Figure 7: **Visual analysis of morphology parameterization.**

#### 4.4 Ablation Studies

In this section, we evaluate the key components of our framework by ablating the morphology parameterization and supervision signals.

**Effects of morphology parameterization** We first analyze the effect of our morphology parameterization by comparing it against a *naïve model* that defines each canonical vertex  $\mathbf{v}_k \in \mathbb{R}^3$  as a free variable in the global coordinate, rather than as a local offset  $\mathbf{o}_k$  relative to the skeleton-dependent anchor  $\mathbf{p}_k$  (Eq. 5). Without the anchor  $\mathbf{p}_k$  coupling  $\mathbf{v}_k$  to the bone lengths  $\ell_b$ , individual vertices can shift independently of the kinematic structure during optimization. As shown in Tab. 3 and Fig. 7, this leads to significant performance degradation (PMD 8.45, FVMD 17.54).

We further ablate individual morphology parameters by progressively enabling them. Without morphology adaptation (fixed morphology), the optimizer compensates for the shape gap through incorrect joint rotations, degrading pose accuracy (PMD 3.72). Enabling bone lengths  $\ell_b$  and global scale  $s_{\text{global}}$  resolves skeletal proportion and scale mismatches, respectively, yielding substantial gains. Offsets  $\mathbf{o}_k$  provide further refinement by capturing residual surface details.

**Effects of supervision losses** Rendering losses alone recover coarse motion but lack part-level precision (PMD 4.52). Adding keypoint supervision  $\mathcal{L}_{\text{keyp}}$  and synthesized-view guidance  $\mathcal{L}_{\text{mv}}$  yields consistent gains, confirming their complementary roles in improving robustness. Extended ablation studies on supervision losses are provided in the appendix.

## 5 Conclusion and Future Work

In this study, we have presented MorphGS, a video-to-3D motion transfer framework. By formulating motion retargeting as an inverse-graphics optimization framework, our approach explicitly factorizes morphology and rig-driven pose parameters. This parameterization effectively addresses source-target shape misalignments, enabling motion transfer without relying on predefined parametric templates or intermediate 3D source reconstruction.

Although our morphology adaptation facilitates cross-identity motion transfer, the current framework assumes a compatible articulated topology between the source and target. This assumption inherently limits transfer across subjects with significantly different kinematic structures. For future work, integrating physics-based motion priors could provide stronger constraints to resolve ambiguities under severe self-occlusions and reduce temporal artifacts. Moreover, explicitly modeling non-rigid soft-tissue deformations could further

improve the expressiveness of the transferred motion. We hope our approach provides a useful step toward more flexible 3D content creation and cross-category motion understanding.

## References

- [1] Pexels: Free stock photos and videos. <https://www.pexels.com>, 2024. Accessed: 2024-10-01.
- [2] Kfir Aberman, Peizhuo Li, Dani Lischinski, Olga Sorkine-Hornung, Daniel Cohen-Or, and Baoquan Chen. Skeleton-aware networks for deep motion retargeting. *ACM Transactions on Graphics (TOG)*, 39(4):62–1, 2020.
- [3] Adobe. Mixamo. <https://www.mixamo.com>.
- [4] Mehmet Aygun and Oisin Mac Aodha. Saor: Single-view articulated object reconstruction. In *Proceedings of the IEEE/CVF Conference on Computer Vision and Pattern Recognition*, pages 10382–10391, 2024.
- [5] Ilya Baran and Jovan Popović. Automatic rigging and animation of 3d characters. *ACM Transactions on graphics (TOG)*, 26(3):72–es, 2007.
- [6] Deniz Beker, Hiroharu Kato, Mihai Adrian Morariu, Takahiro Ando, Toru Matsuoka, Wadim Kehl, and Adrien Gaidon. Monocular differentiable rendering for self-supervised 3d object detection. In *European conference on computer vision*, pages 514–529. Springer, 2020.
- [7] Mark Boss, Zixuan Huang, Aaryaman Vasishtha, and Varun Jampani. Sf3d: Stable fast 3d mesh reconstruction with uv-unwrapping and illumination disentanglement. In *Proceedings of the Computer Vision and Pattern Recognition Conference*, pages 16240–16250, 2025.
- [8] Jinnan Chen, Chen Li, and Gim Hee Lee. Weakly-supervised 3d pose transfer with keypoints. In *Proceedings of the IEEE/CVF International Conference on Computer Vision*, pages 15156–15165, 2023.
- [9] Haoqiang Fan, Hao Su, and Leonidas J Guibas. A point set generation network for 3d object reconstruction from a single image. In *Proceedings of the IEEE conference on computer vision and pattern recognition*, pages 605–613, 2017.
- [10] Zhoujie Fu, Jiacheng Wei, Wenhao Shen, Chaoyue Song, Xiaofeng Yang, Fayao Liu, Xulei Yang, and Guosheng Lin. Sync4d: Video guided controllable dynamics for physics-based 4d generation. *arXiv preprint arXiv:2405.16849*, 2024.
- [11] Lin Gao, Jie Yang, Yi-Ling Qiao, Yu-Kun Lai, Paul L Rosin, Weiwei Xu, and Shihong Xia. Automatic unpaired shape deformation transfer. *ACM Transactions on Graphics (ToG)*, 37(6):1–15, 2018.
- [12] Michael Gleicher. Retargetting motion to new characters. In *Proceedings of the 25th annual conference on Computer graphics and interactive techniques*, pages 33–42, 1998.
- [13] Shubham Goel, Georgios Pavlakos, Jathushan Rajasegaran, Angjoo Kanazawa, and Jitendra Malik. Humans in 4d: Reconstructing and tracking humans with transformers. In *Proceedings of the IEEE/CVF International Conference on Computer Vision*, pages 14783–14794, 2023.
- [14] Liangxiao Hu, Hongwen Zhang, Yuxiang Zhang, Boyao Zhou, Boning Liu, Shengping Zhang, and Liqiang Nie. Gaussianavatar: Towards realistic human avatar modeling from a single video via animatable 3d gaussians. In *Proceedings of the IEEE/CVF Conference on Computer Vision and Pattern Recognition (CVPR)*, pages 634–644, June 2024.
- [15] Yi-Hua Huang, Yang-Tian Sun, Ziyi Yang, Xiaoyang Lyu, Yan-Pei Cao, and Xiaojuan Qi. Sc-gs: Sparse-controlled gaussian splatting for editable dynamic scenes. In *Proceedings of the IEEE/CVF Conference on Computer Vision and Pattern Recognition (CVPR)*, pages 4220–4230, June 2024.

- [16] Tomas Jakab, Ruining Li, Shangzhe Wu, Christian Rupprecht, and Andrea Vedaldi. Farm3d: Learning articulated 3d animals by distilling 2d diffusion. In *2024 International Conference on 3D Vision (3DV)*, pages 852–861. IEEE, 2024.
- [17] Angjoo Kanazawa, Michael J. Black, David W. Jacobs, and Jitendra Malik. End-to-end recovery of human shape and pose. In *Computer Vision and Pattern Recognition (CVPR)*, 2018.
- [18] Bernhard Kerbl, Georgios Kopanas, Thomas Leimkühler, and George Drettakis. 3d gaussian splatting for real-time radiance field rendering. *ACM Trans. Graph.*, 42(4):139–1, 2023.
- [19] Diederik P Kingma and Jimmy Ba. Adam: A method for stochastic optimization. *arXiv preprint arXiv:1412.6980*, 2014.
- [20] Onorina Kovalenko, Vladislav Golyanik, Jameel Malik, Ahmed Elhayek, and Didier Stricker. Structure from articulated motion: accurate and stable monocular 3d reconstruction without training data. *Sensors*, 19(20):4603, 2019.
- [21] Alexander Krull, Eric Brachmann, Frank Michel, Michael Ying Yang, Stefan Gumhold, and Carsten Rother. Learning analysis-by-synthesis for 6d pose estimation in rgb-d images. In *Proceedings of the IEEE international conference on computer vision*, pages 954–962, 2015.
- [22] Yang Li, Hikari Takehara, Takafumi Taketomi, Bo Zheng, and Matthias Nießner. 4dcomplete: Non-rigid motion estimation beyond the observable surface. In *Proceedings of the IEEE/CVF International Conference on Computer Vision*, pages 12706–12716, 2021.
- [23] Zhiqi Li, Yiming Chen, and Peidong Liu. Dreammesh4d: Video-to-4d generation with sparse-controlled gaussian-mesh hybrid representation. *Advances in Neural Information Processing Systems*, 37:21377–21400, 2024.
- [24] Zizhang Li, Dor Litvak, Ruining Li, Yunzhi Zhang, Tomas Jakab, Christian Rupprecht, Shangzhe Wu, Andrea Vedaldi, and Jiajun Wu. Learning the 3d fauna of the web. In *Proceedings of the IEEE/CVF Conference on Computer Vision and Pattern Recognition*, pages 9752–9762, 2024.
- [25] Zhouyingcheng Liao, Jimei Yang, Jun Saito, Gerard Pons-Moll, and Yang Zhou. Skeleton-free pose transfer for stylized 3d characters. In *European Conference on Computer Vision*, pages 640–656. Springer, 2022.
- [26] Jiahe Liu, Youran Qu, Qi Yan, Xiaohui Zeng, Lele Wang, and Renjie Liao. Fr\`echet video motion distance: A metric for evaluating motion consistency in videos. *arXiv preprint arXiv:2407.16124*, 2024.
- [27] Ruoshi Liu, Rundi Wu, Basile Van Hoorick, Pavel Tokmakov, Sergey Zakharov, and Carl Vondrick. Zero-1-to-3: Zero-shot one image to 3d object. In *Proceedings of the IEEE/CVF international conference on computer vision*, pages 9298–9309, 2023.
- [28] Matthew Loper, Naureen Mahmood, Javier Romero, Gerard Pons-Moll, and Michael J. Black. SMPL: A skinned multi-person linear model. *ACM Trans. Graphics (Proc. SIGGRAPH Asia)*, 34(6):248:1–248:16, October 2015.
- [29] Jin Lyu, Tianyi Zhu, Yi Gu, Li Lin, Pujin Cheng, Yebin Liu, Xiaoying Tang, and Liang An. Animer: Animal pose and shape estimation using family aware transformer. *arXiv preprint arXiv:2412.00837*, 2024.
- [30] Shubh Maheshwari, Rahul Narain, and Ramya Hebbalaguppe. Transfer4d: A framework for frugal motion capture and deformation transfer. In *Proceedings of the IEEE/CVF Conference on Computer Vision and Pattern Recognition*, pages 12836–12846, 2023.
- [31] Ben Mildenhall, Pratul P Srinivasan, Matthew Tancik, Jonathan T Barron, Ravi Ramamoorthi, and Ren Ng. Nerf: Representing scenes as neural radiance fields for view synthesis. *Communications of the ACM*, 65(1):99–106, 2021.

- [32] Sanjeev Muralikrishnan, Niladri Dutt, Siddhartha Chaudhuri, Noam Aigerman, Vladimir Kim, Matthew Fisher, and Niloy J Mitra. Temporal residual jacobians for rig-free motion transfer. In *European Conference on Computer Vision*, pages 93–109. Springer, 2024.
- [33] Maxime Oquab, Timothée Darcet, Théo Moutakanni, Huy Vo, Marc Szafraniec, Vasil Khalidov, Pierre Fernandez, Daniel Haziza, Francisco Massa, Alaaeldin El-Nouby, et al. Dinov2: Learning robust visual features without supervision. *arXiv preprint arXiv:2304.07193*, 2023.
- [34] Federico Perazzi, Jordi Pont-Tuset, Brian McWilliams, Luc Van Gool, Markus Gross, and Alexander Sorkine-Hornung. A benchmark dataset and evaluation methodology for video object segmentation. In *Proceedings of the IEEE conference on computer vision and pattern recognition*, pages 724–732, 2016.
- [35] Conrad J Poelman and Takeo Kanade. A paraperspective factorization method for shape and motion recovery. *IEEE transactions on pattern analysis and machine intelligence*, 19(3):206–218, 1997.
- [36] Nikhila Ravi, Jeremy Reizenstein, David Novotny, Taylor Gordon, Wan-Yen Lo, Justin Johnson, and Georgia Gkioxari. Accelerating 3d deep learning with pytorch3d. *arXiv:2007.08501*, 2020.
- [37] Helge Rhodin, Jörg Spörri, Isinsu Katircioglu, Victor Constantin, Frédéric Meyer, Erich Müller, Mathieu Salzmann, and Pascal Fua. Learning monocular 3d human pose estimation from multi-view images. In *Proceedings of the IEEE conference on computer vision and pattern recognition*, pages 8437–8446, 2018.
- [38] Nadine Rueegg, Silvia Zuffi, Konrad Schindler, and Michael J Black. Barc: Learning to regress 3d dog shape from images by exploiting breed information. In *Proceedings of the IEEE/CVF Conference on Computer Vision and Pattern Recognition*, pages 3876–3884, 2022.
- [39] Nadine Rüegg, Shashank Tripathi, Konrad Schindler, Michael J Black, and Silvia Zuffi. Bite: Beyond priors for improved three-d dog pose estimation. In *Proceedings of the IEEE/CVF Conference on Computer Vision and Pattern Recognition*, pages 8867–8876, 2023.
- [40] Remy Sabathier, Niloy J. Mitra, and David Novotny. Animal avatars: Reconstructing animatable 3d animals from casual videos. In *Computer Vision – ECCV 2024: 18th European Conference, Milan, Italy, September 29–October 4, 2024, Proceedings, Part LXXIX*, page 270–287, 2024.
- [41] Aleksandar Shtedritski, Christian Rupprecht, and Andrea Vedaldi. Shic: Shape-image correspondences with no keypoint supervision. In *ECCV*, 2024.
- [42] Oriane Siméoni, Huy V. Vo, Maximilian Seitzer, Federico Baldassarre, Maxime Oquab, Cijo Jose, Vasil Khalidov, Marc Szafraniec, Seungeun Yi, Michaël Ramamonjisoa, Francisco Massa, Daniel Haziza, Luca Wehrstedt, Jianyuan Wang, Timothée Darcet, Théo Moutakanni, Leonel Sentana, Claire Roberts, Andrea Vedaldi, Jamie Tolan, John Brandt, Camille Couprie, Julien Mairal, Hervé Jégou, Patrick Labatut, and Piotr Bojanowski. DINOv3, 2025.
- [43] Chaoyue Song, Xiu Li, Fan Yang, Zhongcong Xu, Jiacheng Wei, Fayao Liu, Jiashi Feng, Guosheng Lin, and Jianfeng Zhang. Puppeteer: Rig and animate your 3d models. *arXiv preprint arXiv:2508.10898*, 2025.
- [44] Chaoyue Song, Jianfeng Zhang, Xiu Li, Fan Yang, Yiwen Chen, Zhongcong Xu, Jun Hao Liew, Xiaoyang Guo, Fayao Liu, Jiashi Feng, et al. Magicarticulate: Make your 3d models articulation-ready. In *Proceedings of the Computer Vision and Pattern Recognition Conference*, pages 15998–16007, 2025.
- [45] Carlo Tomasi and Takeo Kanade. Shape and motion from image streams under orthography: a factorization method. *International journal of computer vision*, 9(2):137–154, 1992.
- [46] Lukas Uzolas, Elmar Eisemann, and Petr Kellnhofer. Template-free articulated neural point clouds for reposable view synthesis. *Advances in Neural Information Processing Systems*, 36:31621–31637, 2023.
- [47] Ashish Vaswani, Noam Shazeer, Niki Parmar, Jakob Uszkoreit, Llion Jones, Aidan N Gomez, Łukasz Kaiser, and Illia Polosukhin. Attention is all you need. *Advances in neural information processing systems*, 30, 2017.

- [48] Ruben Villegas, Duygu Ceylan, Aaron Hertzmann, Jimei Yang, and Jun Saito. Contact-aware retargeting of skinned motion. In *Proceedings of the IEEE/CVF International Conference on Computer Vision*, pages 9720–9729, 2021.
- [49] Ruben Villegas, Jimei Yang, Duygu Ceylan, and Honglak Lee. Neural kinematic networks for unsupervised motion retargeting. In *Proceedings of the IEEE conference on computer vision and pattern recognition*, pages 8639–8648, 2018.
- [50] Angtian Wang, Wufei Ma, Alan Yuille, and Adam Kortylewski. Neural textured deformable meshes for robust analysis-by-synthesis. In *Proceedings of the IEEE/CVF Winter Conference on Applications of Computer Vision*, pages 3108–3117, 2024.
- [51] Jiashun Wang, Xueting Li, Sifei Liu, Shalini De Mello, Orazio Gallo, Xiaolong Wang, and Jan Kautz. Zero-shot pose transfer for unrigged stylized 3d characters. In *Proceedings of the IEEE/CVF Conference on Computer Vision and Pattern Recognition*, pages 8704–8714, 2023.
- [52] Jiashun Wang, Chao Wen, Yanwei Fu, Haitao Lin, Tianyun Zou, Xiangyang Xue, and Yinda Zhang. Neural pose transfer by spatially adaptive instance normalization. In *Proceedings of the IEEE/CVF conference on computer vision and pattern recognition*, pages 5831–5839, 2020.
- [53] Yilin Wang, Chuan Guo, Yuxuan Mu, Muhammad Gohar Javed, Xinxin Zuo, Juwei Lu, Hai Jiang, and Li Cheng. Motiondreamer: One-to-many motion synthesis with localized generative masked transformer. *arXiv preprint arXiv:2504.08959*, 2025.
- [54] Guanjun Wu, Taoran Yi, Jiemin Fang, Lingxi Xie, Xiaopeng Zhang, Wei Wei, Wenyu Liu, Qi Tian, and Xinggang Wang. 4d gaussian splatting for real-time dynamic scene rendering. In *Proceedings of the IEEE/CVF Conference on Computer Vision and Pattern Recognition (CVPR)*, pages 20310–20320, June 2024.
- [55] Shangzhe Wu, Tomas Jakab, Christian Rupprecht, and Andrea Vedaldi. Dove: Learning deformable 3d objects by watching videos. *International Journal of Computer Vision*, 131(10):2623–2634, 2023.
- [56] Shangzhe Wu, Ruining Li, Tomas Jakab, Christian Rupprecht, and Andrea Vedaldi. Magicpony: Learning articulated 3d animals in the wild. In *Proceedings of the IEEE/CVF Conference on Computer Vision and Pattern Recognition*, pages 8792–8802, 2023.
- [57] Zijie Wu, Chaohui Yu, Yanqin Jiang, Chenjie Cao, Fan Wang, and Xiang Bai. Sc4d: Sparse-controlled video-to-4d generation and motion transfer. In *European Conference on Computer Vision*, pages 361–379. Springer, 2024.
- [58] Jing Xiao, Jin-xiang Chai, and Takeo Kanade. A closed-form solution to non-rigid shape and motion recovery. In *European conference on computer vision*, pages 573–587. Springer, 2004.
- [59] Zhan Xu, Yang Zhou, Evangelos Kalogerakis, Chris Landreth, and Karan Singh. Rignet: Neural rigging for articulated characters. *arXiv preprint arXiv:2005.00559*, 2020.
- [60] Gengshan Yang, Minh Vo, Natalia Neverova, Deva Ramanan, Andrea Vedaldi, and Hanbyul Joo. Banmo: Building animatable 3d neural models from many casual videos. In *Proceedings of the IEEE/CVF Conference on Computer Vision and Pattern Recognition*, pages 2863–2873, 2022.
- [61] Chun-Han Yao, Wei-Chih Hung, Yuanzhen Li, Michael Rubinstein, Ming-Hsuan Yang, and Varun Jampani. Lassie: Learning articulated shapes from sparse image ensemble via 3d part discovery. *Advances in Neural Information Processing Systems*, 35:15296–15308, 2022.
- [62] Chun-Han Yao, Yiming Xie, Vikram Voleti, Huaizu Jiang, and Varun Jampani. Sv4d 2.0: Enhancing spatio-temporal consistency in multi-view video diffusion for high-quality 4d generation. In *Proceedings of the IEEE/CVF International Conference on Computer Vision*, pages 13248–13258, 2025.
- [63] Yuxin Yao, Zhi Deng, and Junhui Hou. Riggs: Rigging of 3d gaussians for modeling articulated objects in videos. In *The IEEE/CVF Conference on Computer Vision and Pattern Recognition*, 2025.

- [64] Xinyu Yi, Yuxiao Zhou, Marc Habermann, Soshi Shimada, Vladislav Golyanik, Christian Theobalt, and Feng Xu. Physical inertial poser (pip): Physics-aware real-time human motion tracking from sparse inertial sensors. In *IEEE/CVF Conference on Computer Vision and Pattern Recognition (CVPR)*, June 2022.
- [65] Seungwoo Yoo, Juil Koo, Kyeongmin Yeo, and Minhyuk Sung. Neural pose representation learning for generating and transferring non-rigid object poses. *arXiv preprint arXiv:2406.09728*, 2024.
- [66] Hao Zhang, Di Chang, Fang Li, Mohammad Soleymani, and Narendra Ahuja. Magicpose4d: Crafting articulated models with appearance and motion control. *arXiv preprint arXiv:2405.14017*, 2024.
- [67] Hongwen Zhang, Yating Tian, Xinchu Zhou, Wanli Ouyang, Yebin Liu, Limin Wang, and Zhenan Sun. Pymaf: 3d human pose and shape regression with pyramidal mesh alignment feedback loop. In *Proceedings of the IEEE/CVF international conference on computer vision*, pages 11446–11456, 2021.
- [68] Jia-Peng Zhang, Cheng-Feng Pu, Meng-Hao Guo, Yan-Pei Cao, and Shi-Min Hu. One model to rig them all: Diverse skeleton rigging with unirig. *arXiv preprint arXiv:2504.12451*, 2025.
- [69] Junyi Zhang, Charles Herrmann, Junhwa Hur, Eric Chen, Varun Jampani, Deqing Sun, and Ming-Hsuan Yang. Telling left from right: Identifying geometry-aware semantic correspondence. In *Proceedings of the IEEE/CVF Conference on Computer Vision and Pattern Recognition*, pages 3076–3085, 2024.
- [70] Tongjie Y Zhang and Ching Y. Suen. A fast parallel algorithm for thinning digital patterns. *Communications of the ACM*, 27(3):236–239, 1984.
- [71] Keyang Zhou, Bharat Lal Bhatnagar, and Gerard Pons-Moll. Unsupervised shape and pose disentanglement for 3d meshes. In *Computer Vision—ECCV 2020: 16th European Conference, Glasgow, UK, August 23–28, 2020, Proceedings, Part XXII 16*, pages 341–357. Springer, 2020.
- [72] Silvia Zuffi, Angjoo Kanazawa, David W Jacobs, and Michael J Black. 3d menagerie: Modeling the 3d shape and pose of animals. In *Proceedings of the IEEE conference on computer vision and pattern recognition*, pages 6365–6373, 2017.

## Appendix

In this appendix, we provide implementation details (Sec. A), extended ablation studies (Sec. B), analysis of morphology adaptation (Sec. C), identifiability analysis of the proposed morphology parameterization (Sec. D), and per-scene quantitative results (Sec. E).

### A Implementation Details

#### A.1 Training objective and regularization

Following Sec. 3.4 of the main paper, we optimize the following objective at each frame:

$$\mathcal{L}_t = \lambda_{\text{render}}(\mathcal{L}_{\text{render}} + \lambda_{\text{mv}}\mathcal{L}_{\text{mv}}) + \lambda_{\text{keyp}}\mathcal{L}_{\text{keyp}} + \mathcal{L}_{\text{reg}}, \quad (14)$$

where  $\mathcal{L}_{\text{reg}} = \mathcal{L}_{\text{smooth}} + \mathcal{L}_{\text{chamf}} + \mathcal{L}_{\text{trans}} + \mathcal{L}_{\text{arap}}$ . We define each term below.

**Temporal smoothness** To discourage abrupt changes over time, we further impose an  $l_1$  penalty on frame-to-frame differences in the joint motion parameters  $\boldsymbol{\theta}_j^t$  and the root translation  $\boldsymbol{\delta}_{\text{root}}^t$ :

$$\mathcal{L}_{\text{smooth}} = \lambda_{\text{smooth}} \left( \sum_{j=1}^J \|\boldsymbol{\theta}_j^t - \boldsymbol{\theta}_j^{t-1}\|_1 + \|\boldsymbol{\delta}_{\text{root}}^t - \boldsymbol{\delta}_{\text{root}}^{t-1}\|_1 \right), \quad (15)$$

where  $\lambda_{\text{smooth}}$  is the loss weight.

**2D Chamfer distance** Following Yao et al. [63], we use a 2D Chamfer distance to align the deformed 3D skeleton with the source silhouette structure in the image plane. Specifically, let  $\mathcal{S}_t$  denote the 2D skeleton point set extracted from the source foreground mask  $\Omega_t$  by morphological thinning [70]. We sample 3D points  $c^t$  on the deformed skeleton and project them to the image plane with  $\pi_t$ , yielding the projected point set  $\hat{\mathcal{S}}_t = \pi_t(c^t)$ :

$$\mathcal{L}_{\text{chamf}} = \lambda_{\text{chamf}} \text{CD}_{l_1}(\mathcal{S}_t, \hat{\mathcal{S}}_t), \quad (16)$$

where  $\text{CD}_{l_1}$  denotes the Chamfer distance [9] under the  $l_1$  norm, and  $\lambda_{\text{chamf}}$  is the corresponding loss weight.

**Transformation regularization** To discourage excessive joint rotation angles and root translations, we impose an  $l_1$  penalty on the per-frame root translation and joint rotation angles. Let  $\boldsymbol{\theta}_j^t = \alpha_j^t \hat{\mathbf{u}}_j^t$  denote the axis-angle pose parameter of joint  $j$  at frame  $t$ , where  $\alpha_j^t$  is the rotation angle and  $\hat{\mathbf{u}}_j^t$  is the unit rotation axis.

$$\mathcal{L}_{\text{trans}} = \lambda_{\text{trans}} \frac{\|\boldsymbol{\delta}_{\text{root}}^t\|_1 + \sum_{j=1}^J |\alpha_j^t|}{J}. \quad (17)$$

Here,  $\lambda_{\text{trans}}$  is the loss weight,  $\boldsymbol{\delta}_{\text{root}}^t$  is the root translation at frame  $t$ , and  $J$  is the number of joints.

**As-Rigid-As-Possible** We use an ARAP loss defined on canonical nearest-neighbor pairs. For each Gaussian  $k$ , the neighborhood  $\mathcal{N}(k)$  is defined in the canonical pose using the canonical Gaussian centers  $\bar{\mathbf{v}}_k$ . We then penalize deviations between the canonical distances  $\|\bar{\mathbf{v}}_k - \bar{\mathbf{v}}_n\|$  and the posed distances  $\|\mathbf{v}_k^t - \mathbf{v}_n^t\|$  for  $n \in \mathcal{N}(k)$ , where  $\mathbf{v}_k^t$  denotes the center of Gaussian  $k$  at frame  $t$ :

$$\mathcal{L}_{\text{arap}} = \lambda_{\text{arap}} \frac{1}{K} \sum_{k=1}^K \frac{1}{|\mathcal{N}(k)|} \sum_{n \in \mathcal{N}(k)} \log \left( 1 + \|\bar{\mathbf{v}}_k - \bar{\mathbf{v}}_n\| - \|\mathbf{v}_k^t - \mathbf{v}_n^t\| \right), \quad (18)$$

We use the  $\log(1 + \cdot)$  form to reduce the contribution of larger discrepancies.

**Loss weights** For Eq. 14, we use  $\lambda_{\text{render}} = 1.0$ ,  $\lambda_{\text{mv}} = 0.25$ , and  $\lambda_{\text{keyp}} = 0.006$ . For motion regularization, we use  $\lambda_{\text{trans}} = 0.005$ ,  $\lambda_{\text{smooth}} = 0.01$ ,  $\lambda_{\text{chamf}} = 0.001$ , and  $\lambda_{\text{arap}} = 1.0$ .

Table A1: **Effect of semantic feature extractors.** PMD ( $\times 10^3$ ,  $\downarrow$ ) and FVMD ( $\times 10^{-3}$ ,  $\downarrow$ ) for different frozen semantic feature extractors show that Geo-Aware yields the best overall results by resolving the inherent geometric left-right ambiguity.

Method	PMD	FVMD
DINOv2 [33]	2.90	9.45
DINOv3 [42]	2.19	9.42
Geo-Aware [69]	<b>1.91</b>	<b>8.82</b>

Table A2: **Effect of correspondence density.** PMD ( $\times 10^3$ ,  $\downarrow$ ) and FVMD ( $\times 10^{-3}$ ,  $\downarrow$ ) remain stable as the retained ratio of sampled correspondences decreases from 100% to 10%.

Ratio (%)	PMD	FVMD
100	<b>1.91</b>	<b>8.82</b>
50	1.94	9.05
30	1.95	9.14
10	1.96	9.36

Table A3: **Analysis on synthesized-view supervision.** PMD ( $\times 10^3$ ,  $\downarrow$ ) and FVMD ( $\times 10^{-3}$ ,  $\downarrow$ ) improve consistently as the number of synthesized views increases.

#Synth. views	PMD	FVMD
0 (w/o $\mathcal{L}_{mv}$ )	2.96	11.93
1	2.27	11.21
2	2.18	9.41
4	1.91	8.82
8	<b>1.85</b>	<b>7.97</b>

## A.2 Model and optimization details

**Pose network** The pose network is an MLP-based motion field following Uzolas et al. [46]. A scalar time input is encoded with a sinusoidal positional embedding and mapped to a 30D latent code by a small time encoder. This code is processed by an 8-layer MLP with 256 hidden units and a skip connection. Two linear heads predict the global 3D translation and per-joint axis-angle rotations. These are converted to joint  $SE(3)$  transforms via Rodrigues’ formula and skeletal kinematics, and applied using linear blend skinning.

**Optimization details** We use learning rates of 0.005, 0.01, and 0.001 for the motion network, global scale, and bone lengths, respectively. Bone lengths are optimized from the start of training, with a step decay of 0.1 applied every 1K iterations, starting at iteration 1K. For Gaussian attributes including offsets, we use the default learning-rate settings of 3D Gaussian Splatting [18].

## A.3 Camera and synthesized-view setup

**Camera setup** In all experiments, we render the posed target from a fixed reference camera chosen from the predefined canonical views of the target mesh, with intrinsics kept fixed throughout optimization. Instead, frame-wise source–target alignment is modeled by a per-frame root transform in  $SE(3)$ . The same setup is used for both synthetic and real videos regardlessly. For synthesized-view guidance, auxiliary views are rendered by rotating the fixed reference camera around the object center by the prescribed azimuth offset [62], while keeping the intrinsics unchanged.

## B Extended Ablation Studies

We extend the ablation studies in Sec. 4.4 of the main paper with additional analysis on design choices. All experiments are conducted on the Mixamo dataset unless otherwise noted.

**Geometry-aware semantic features** Distinguishing semantically similar but geometrically different parts, such as left and right limbs, is important for accurate correspondence matching. We therefore use a pretrained geometry-aware semantic feature extractor (Geo-Aware) [69]. We compare Geo-Aware, DINOv2 [33], and DINOv3 [42] while keeping the rest of the optimization pipeline fixed. All feature extractors are used frozen. Tab. A1 shows that Geo-Aware achieves the lowest PMD and FVMD among the compared variants, indicating that features trained to resolve left-right ambiguity are better suited to our motion learning setting.

**Keypoint density** We further vary the density of keypoint supervision by randomly retaining a fraction of the 1K sampled correspondences per frame. As shown in Tab. A2, reducing the retained ratio from 100% to 10% causes only a modest degradation, with PMD increasing from 1.91 to 1.96 (+2.6%) and FVMD from 8.82 to 9.36 (+6.1%). This indicates that the sampled correspondences mainly constrain coarse part-level alignment rather than fine-grained geometry. Once this alignment is provided, further increasing the correspondence density has a limited effect on the final result.

Table A4: **Effect of target rig initialization.** Results on DT4D-Quadrupeds with different auto-rigging methods used to initialize the target rig. PMD ( $\times 10^3$ ,  $\downarrow$ ) and FVMD ( $\times 10^{-3}$ ,  $\downarrow$ ) vary with the choice of rig initializer.

Method	PMD	FVMD
MorphGS + Pinocchio [5]	1.49	9.79
MorphGS + RigNet [59]	1.33	8.81
MorphGS + MagicArticulate [44]	1.21	8.94
MorphGS + Puppeteer [43]	<b>1.14</b>	<b>8.62</b>

Table A5: **Effect of pose parameterization.** Comparison between direct per-frame pose optimization and a time-conditioned pose network. The pose network yields lower PMD ( $\times 10^3$ ), FVMD ( $\times 10^{-3}$ ), and Jitter ( $\text{km/s}^3$ ) than per-frame pose optimization.

Method	PMD	FVMD	Jitter
Per-frame Pose	2.60	12.98	0.15
Pose Network	<b>1.91</b>	<b>8.82</b>	<b>0.09</b>

Table A6: **Quantitative evaluation of adapted skeletons on two character pairs.** MPJPE is measured in the rest pose. PCK@0.1 and PCK@0.2 use thresholds of 10% and 20% of the characteristic length ( $L_{\text{char}} = \sqrt[3]{V_{\text{GT}}}$ ), respectively.

Method	Mannequin $\rightarrow$ Ortiz			Mannequin $\rightarrow$ Pumpkinhulk		
	MPJPE $\downarrow$	PCK@0.1 $\uparrow$	PCK@0.2 $\uparrow$	MPJPE $\downarrow$	PCK@0.1 $\uparrow$	PCK@0.2 $\uparrow$
Pinocchio [5]	0.1013	0.6316	0.8947	0.1280	0.3684	0.8947
Ours	<b>0.0736</b>	<b>0.7368</b>	<b>0.9868</b>	<b>0.0790</b>	<b>0.6316</b>	<b>0.9605</b>

**Number of synthesized views** Tab. A3 reports the effect of varying the number of synthesized views  $N$  used in  $\mathcal{L}_{\text{mv}}$  (Eq. 13). PMD and FVMD decrease monotonically as  $N$  increases from 0 to 8, confirming that additional viewpoints provide complementary supervision, with diminishing returns beyond  $N = 4$ . We use  $N = 4$  as the default, as increasing to  $N = 8$  yields only a modest further improvement (PMD: 1.91  $\rightarrow$  1.85, FVMD: 8.82  $\rightarrow$  7.97) while increasing the cost of novel-view synthesis. Notably, even without multi-view supervision ( $N = 0$ ), MorphGS achieves PMD of 2.96 and FVMD of 11.93, already matching SPT<sup>+</sup> in PMD and outperforming it in FVMD (12.56), indicating that the rendering and keypoint losses alone provide a competitive baseline.

**Auto-rigging methods** We ablate the target rig initialization used in MorphGS by replacing the off-the-shelf auto-rigging tool [5, 59, 44, 43] while keeping the rest of the optimization unchanged. We report this comparison on DT4D-Quadrupeds [22], focusing on the setting where target rig initialization is required and all compared rigging methods are applicable. As shown in Tab. A4, MorphGS is applicable with multiple auto-rigging methods, while stronger rig initialization leads to better PMD and FVMD.

**Pose network vs. per-frame pose optimization** Tab. A5 compares direct per-frame pose optimization against our time-conditioned pose network (Sec. 3.3). We additionally report *Jitter* [64], the mean jerk of all body joints in global space ( $\text{km/s}^3$ ), which reflects the temporal smoothness of the recovered motion. The pose network outperforms per-frame optimization across all three metrics (PMD: 1.91 vs. 2.60, FVMD: 8.82 vs. 12.98, Jitter: 0.09 vs. 0.15). The gain is consistent with the MLP’s implicit temporal continuity, which encourages motion consistency across adjacent frames and suppresses high-frequency artifacts, as reflected in the lower Jitter score.

## C Analysis of Morphology Adaptation

We analyze whether the optimized morphology parameters yield geometrically meaningful skeletal adaptation. Fig. A1 shows morphology adaptation during optimization. The global scale, bone lengths, and offset vectors are updated from the target initialization.

For evaluation, we measure how closely the adapted target skeleton matches the ground-truth skeleton in the rest pose. We compare against Pinocchio [5], a geometry-driven auto-rigging baseline that fits the target skeleton directly to the source mesh. In contrast, our method adapts the target skeleton solely from the source video, without access to the source 3D geometry. We report normalized Mean Per-Joint Position Error (MPJPE,  $\downarrow$ ) and Percentage of Correct Keypoints (PCK,  $\uparrow$ ) [37] between the adapted skeleton and the ground-truth skeleton. PCK@0.1 and PCK@0.2 use thresholds of 10% and 20% of the characteristic length

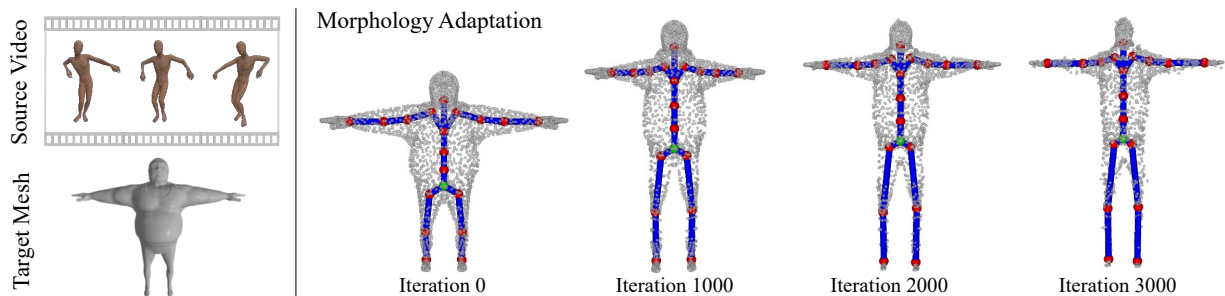


Figure A1: **Visualization of morphology adaptation.** During optimization, the global scale, bone lengths, and offset vectors are updated from the target initialization to better match the source subject.

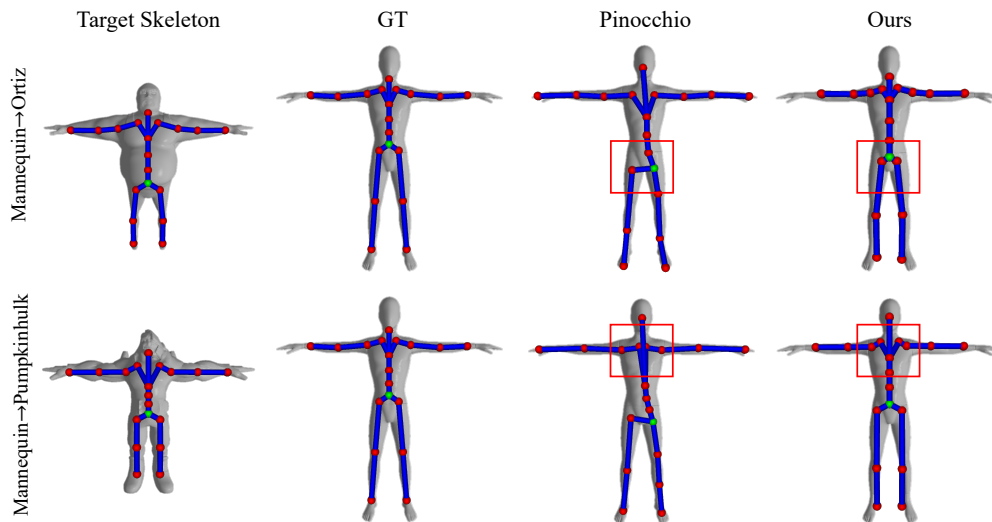


Figure A2: **Qualitative comparison of adapted skeletons in the rest pose.** Joint positions and bones are shown as colored spheres overlaid on the target mesh for two character pairs: Mannequin  $\rightarrow$  Ortiz and Mannequin  $\rightarrow$  Pumpkinhulk. Red boxes highlight the region where our adapted skeleton is more closely aligned with the ground-truth structure.

$L_{\text{char}} = \sqrt[3]{V_{\text{GT}}}$ , where  $V_{\text{GT}}$  denotes the volume of the ground-truth 3D character mesh. For each character pair, the results are averaged over five motion sequences.

As shown in Tab. A6 and Fig. A2, our method yields lower MPJPE and higher PCK than Pinocchio on both character pairs. This indicates that the adapted skeleton is more closely aligned with the ground-truth skeleton, while not requiring the source mesh.

## D Theoretical Analysis of Morphology Parameterization

In this section, we provide an additional theoretical motivation for our morphology parameterization and the staged optimization strategy in Sec. 4.1. By coupling surface geometry to the kinematic chain through a small set of structured parameters, the monocular optimization problem becomes well-constrained: during the early optimization stage where offsets  $\{\mathbf{o}_k\}$  remain fixed (optimization stage 1), the skeletal proportions are identifiable up to a global scale under assumptions on the observed motion. We adopt the notation from the main paper (Eq. 3–6).

## D.1 Setup

Consider a monocular video  $\{I_t\}_{t=1}^T$  of an articulated object observed under weak-perspective projection. The object consists of  $B$  rigid bones forming a kinematic tree  $\mathcal{T}$ . We assume:

- ( $\mathcal{A}_1$ ) **Piecewise rigidity.** Each bone is a rigid body, and its attached surface vertices maintain fixed local-frame positions across all frames. This serves as an idealized approximation of the rig-coupled surface model used in the main method.
- ( $\mathcal{A}_2$ ) **Non-degenerate motion.** Each bone undergoes sufficiently rich motion across the sequence, including rotations about at least two linearly independent axes, and adjacent bones exhibit non-degenerate relative motion. The motion is temporally continuous, so depth ordering does not change discontinuously across consecutive frames.
- ( $\mathcal{A}_3$ ) **Weak-perspective projection with fixed camera.** The camera coordinate frame is fixed. The 2D projection of  $\mathbf{x} = [x, y, z]^\top$  at frame  $t$  is  $\boldsymbol{\pi}_t(\mathbf{x}) = s_f^t [x, y]^\top + \mathbf{t}^t$ , where  $s_f^t > 0$  is a per-frame scale factor and  $\mathbf{t}^t \in \mathbb{R}^2$  is a 2D translation.

With the local offsets  $\{\mathbf{o}_k\}$  fixed from the target rig, the canonical vertex position is derived from morphology parameters:

$$\bar{\mathbf{v}}_k = s_{\text{global}}(\mathbf{p}_k(\{\ell_b\}) + \mathbf{o}_k),$$

as defined in Eq. 5–6 of the main paper. The unknowns thus reduce to the global scale  $s_{\text{global}}$ , bone lengths  $\{\ell_b\}$ , and per-frame joint rotations  $\{\boldsymbol{\theta}_j^t\}$ , which in turn determine the per-bone orientations  $\{\mathbf{R}_b^t\}$  through forward kinematics (Eq. 7–8).

## D.2 Identifiability Statement

Our optimization begins from the target character’s bone proportions and adjusts them to best explain the source video observations. Under the idealized assumptions above, the structured morphology parameterization substantially reduces ambiguity compared with unconstrained vertex-wise deformation. The following proposition states that, in this early stage with fixed offsets, the skeletal morphology is generically identifiable up to a single global scale.

**Proposition 1** (Identifiability of Skeletal Morphology). *Under  $\mathcal{A}_1$ – $\mathcal{A}_3$ , suppose that each bone has at least four non-coplanar associated surface points, and that these points are observed across sufficiently many frames with non-degenerate motion. Then the morphology parameters  $(s_{\text{global}}, \{\ell_b\})$  and the per-frame bone orientations  $\{\mathbf{R}_b^t\}$  are determined by the 2D observations up to a single global scale factor. In particular, all bone-length ratios  $\ell_b/\ell_{b'}$  are uniquely determined.*

## D.3 Proof Sketch of Proposition 1

We now provide a proof sketch of Proposition 1, explaining how the structured morphology parameterization reduces the ambiguity of the monocular reconstruction problem.

**Step 1: Per-bone structure recovery up to a similarity ambiguity** Under  $\mathcal{A}_1$ , each bone  $b$  is associated with a set of surface points whose relative configuration is fixed over time. For such points, the weak-perspective observation at frame  $t$  can be written as

$$\mathbf{u}_k^t = s_f^t \mathbf{R}_{b,2 \times 3}^t \mathbf{v}_k + \mathbf{t}_b^t, \quad (19)$$

where  $s_f^t > 0$  is the per-frame projection scale shared across all bones,  $\mathbf{R}_{b,2 \times 3}^t$  denotes the first two rows of the bone pose in the camera frame, and  $\mathbf{t}_b^t \in \mathbb{R}^2$  collects the projected translation term. Subtracting the per-frame centroid removes translation, yielding:

$$\tilde{\mathbf{u}}_k^t = s_f^t \mathbf{R}_{b,2 \times 3}^t \tilde{\mathbf{v}}_k. \quad (20)$$

Let

$$\mathbf{S}_b = [\tilde{\mathbf{v}}_1 \quad \cdots \quad \tilde{\mathbf{v}}_{P_b}] \in \mathbb{R}^{3 \times P_b} \quad (21)$$

collect the centered 3D point coordinates of bone  $b$ , and let:

$$\mathbf{M}_b = \begin{bmatrix} s_f^1 \mathbf{R}_{b,2 \times 3}^1 \\ s_f^2 \mathbf{R}_{b,2 \times 3}^2 \\ \vdots \\ s_f^T \mathbf{R}_{b,2 \times 3}^T \end{bmatrix} \in \mathbb{R}^{2T \times 3} \quad (22)$$

stack the scaled projected rotations across frames. Then stacking the centered 2D observations over all frames gives the measurement matrix:

$$\tilde{\mathbf{W}}_b = \mathbf{M}_b \mathbf{S}_b, \quad (23)$$

where  $\tilde{\mathbf{W}}_b \in \mathbb{R}^{2T \times P_b}$ . By construction,  $\text{rank}(\tilde{\mathbf{W}}_b) \leq 3$ . Under the stated assumptions, this rank is generically equal to 3. This is because the associated surface points span a three-dimensional local configuration, and the motion is sufficiently rich across frames according to  $\mathcal{A}_2$ . It then follows from standard scaled-orthographic rigid structure-from-motion factorization arguments [45, 35] that  $\tilde{\mathbf{W}}_b$  determines the 3D point configuration of bone  $b$  and its per-frame pose sequence up to a bone-specific similarity ambiguity. Concretely, for each bone one may recover a shape basis and motion matrices that are equivalent to the true ones up to an invertible  $3 \times 3$  transform. After enforcing the metric constraints (i.e., each row pair of  $\mathbf{M}_b$  consists of two orthogonal vectors of equal norm  $s_f^t$ ), the remaining ambiguity reduces to a similarity transform consisting of a scale, a 3D rigid change of coordinates, and possibly a reflection. Temporal continuity helps exclude inconsistent frame-to-frame sign flips, but a per-bone gauge ambiguity still remains at this stage. Therefore, Step 1 recovers each bone only up to an independent similarity class, not yet in a common global frame.

**Step 2: Scale and orientation unification via joint constraints** Adjacent bones are not independent because neighboring bones share joints. If bones  $b$  and  $b'$  share a joint  $j$ , then their reconstructed motions must be consistent with the same joint trajectory across frames. These shared-joint constraints couple the per-bone similarity ambiguities left unresolved in Step 1. Under non-degenerate relative motion ( $\mathcal{A}_2$ ), they fix both the relative scale and relative orientation between adjacent bones, since an incorrect relative scale or an inconsistent reflection would cause the joint trajectories inferred from the two bones to disagree over time. Applying this argument recursively along the kinematic tree unifies all per-bone scales into a single global scale  $\alpha$  and all per-bone reflections into at most a single global reflection. The per-frame projection scale  $s_f^t$  is shared across all bones and cancels in these inter-bone constraints. Finally, temporal continuity ( $\mathcal{A}_2$ ) resolves the remaining global reflection, as only one of the two choices produces a depth trajectory that varies continuously over time.

**Step 3: Bone length recovery** Once the joint trajectories are expressed in a common 3D frame up to the single global scale  $\alpha$ , the length of bone  $b$  is given by the distance between its parent and child joints. Let  $\mathbf{j}^t(j)$  denote the recovered 3D position of joint  $j$  at frame  $t$ . Then

$$\hat{\ell}_b = \|\mathbf{j}^t(j_{\text{child}}) - \mathbf{j}^t(j_{\text{parent}})\|. \quad (24)$$

Because this parent-child distance is invariant for a rigid bone,  $\hat{\ell}_b$  is independent of  $t$  and satisfies

$$\hat{\ell}_b = \alpha \ell_b. \quad (25)$$

Therefore, all bone-length ratios  $\ell_b/\ell_{b'}$  are determined, while the absolute lengths remain ambiguous only up to the single global scale absorbed into  $s_{\text{global}}$ .

**Step 4: Bone orientation and twist disambiguation** The preceding steps determine the joint trajectories and bone lengths in a common 3D frame up to the single global scale. This is sufficient to fix the bone axis of each segment, but not, in general, the rotation about that axis. In other words, recovering orientation from joint positions alone leaves a residual twist ambiguity. This remaining ambiguity is resolved

by the surface observations. Each bone is associated with surface points whose local offsets remain fixed, and these offsets generically include components perpendicular to the bone axis. A twist rotation about the bone axis therefore moves such off-axis points, which in turn changes their projected 2D locations. Consequently, different twist angles produce different image observations. Therefore, under generic non-axisymmetric local surface geometry, the surface observations determine the residual twist angle of each bone. Together with Steps 1–3, this yields the per-frame bone orientations  $\{\mathbf{R}_b^t\}$  uniquely, while the morphology parameters  $(s_{\text{global}}, \{\ell_b\})$  are determined up to the single global scale already accounted for above.  $\square$

#### D.4 Practical Implications

**Effect of structured parameterization.** In a naïve formulation, each vertex  $\bar{\mathbf{v}}_k \in \mathbb{R}^3$  is optimized independently, allowing individual vertices to drift freely regardless of the underlying skeletal structure. Our parameterization instead decomposes each vertex into a skeleton-dependent anchor  $\mathbf{p}_k(\{\ell_b\})$  and a local offset  $\mathbf{o}_k$  (Eq. 5–6), coupling vertex positions to the kinematic chain through bone lengths and skinning weights. As a result, adjusting a single bone length coherently displaces all vertices attached to the affected limb, enforcing that shape changes remain structurally consistent across the body. This kinematic coupling is what enables the identifiability result in Proposition 1: in the early stage where offsets are fixed, the skeletal proportions are determined up to a single global scale from monocular observations alone.

**Fixing offsets in the early stage.** Although our parameterization couples vertex positions to the kinematic chain, a potential ambiguity remains when offsets  $\{\mathbf{o}_k\}$  and bone lengths are optimized simultaneously: a change  $\ell_b \rightarrow \ell_b + \delta\ell_b$  shifts the anchor  $\mathbf{p}_k$  by  $\Delta\mathbf{p}_k$ , which can be compensated by  $\mathbf{o}_k \rightarrow \mathbf{o}_k - \Delta\mathbf{p}_k$ , leaving the canonical vertex position  $\mathbf{v}_k = \mathbf{p}_k + \mathbf{o}_k$  largely unchanged. Fixing the offsets during the early optimization stage, while estimating only the skeletal parameters, removes this potential ambiguity and allows bone lengths to be determined primarily from the observed motion. The offsets are released in the later stage once the skeleton is sufficiently constrained, to capture residual shape details beyond what the skeletal proportions alone can express.

**Role of offsets under morphology mismatch.** The identifiability analysis above relies on idealized assumptions such as piecewise rigidity and weak-perspective projection. In practice, the source and target often differ substantially in local geometry (e.g., limb thickness, torso proportions, or surface details) that skeletal parameters alone cannot account for. The offset parameters  $\{\mathbf{o}_k\}$ , released in the later optimization stage, provide additional representational capacity to accommodate such local shape discrepancies, reducing the model mismatch between the rig-based representation and the actual source appearance observed in the video.

## E Quantitative Evaluations

We provide detailed quantitative results for all evaluation scenes from the Mixamo [3] and DT4D [22] datasets in Tab. A7, Tab. A8, and Tab. A9.

Table A7: **Quantitative evaluation across all scenes from the Mixamo dataset.** PMD and FVMD values are reported in  $10^3$  and  $10^{-3}$  scales, respectively. Lower is better. Best and second-best results are highlighted in red and orange, respectively.

Method	JumpingJacks		Running		SideStep		SkinningTest		StandingJump		SwingDance	
	PMD	FVMD	PMD	FVMD	PMD	FVMD	PMD	FVMD	PMD	FVMD	PMD	FVMD
SPT <sup>+</sup>	0.79	8.55	2.08	11.27	1.68	6.68	2.48	20.14	4.28	24.15	1.69	7.25
NPR <sup>+</sup>	0.85	8.63	2.80	16.11	1.62	21.01	6.93	24.00	5.51	32.04	1.71	8.99
Transfer4D	6.14	16.27	5.66	17.92	1.61	25.50	5.56	18.77	9.62	24.12	2.56	11.09
Pinocchio <sup>+</sup>	15.58	18.46	2.76	10.64	1.16	7.37	2.50	17.85	4.55	26.96	1.61	11.33
Ours	0.39	4.19	1.54	6.54	1.03	6.84	1.71	17.66	5.08	22.55	1.04	5.74

Method	Walking		Floating		HipHopDance		Header		Dying		Snatch	
	PMD	FVMD	PMD	FVMD	PMD	FVMD	PMD	FVMD	PMD	FVMD	PMD	FVMD
SPT <sup>+</sup>	1.83	6.07	5.08	10.20	1.51	8.25	4.86	7.80	5.50	7.88	3.71	32.46
NPR <sup>+</sup>	2.97	9.55	4.20	11.35	1.64	10.22	5.44	8.87	8.95	9.24	5.17	39.98
Transfer4D	7.16	12.44	13.89	7.40	2.75	11.57	19.08	6.90	6.38	8.19	11.40	33.70
Pinocchio <sup>+</sup>	2.32	6.83	2.79	11.10	1.36	7.80	5.20	11.32	3.15	5.05	11.61	33.70
Ours	0.93	4.11	1.97	7.63	0.60	6.82	3.11	6.81	3.08	5.38	2.44	11.52

Table A8: **Quantitative evaluation across all scenes from DT4D-Quadrupeds.** PMD and FVMD values are reported in  $10^3$  and  $10^{-3}$  scales, respectively. Lower is better. Best and second-best results are highlighted in red and orange, respectively.

Method	Punch		Walk1		Death		Walk2		KickBack	
	PMD	FVMD	PMD	FVMD	PMD	FVMD	PMD	FVMD	PMD	FVMD
NPR <sup>+</sup>	2.92	8.48	2.32	23.23	5.31	27.51	1.27	8.64	2.95	20.61
Transfer4D	4.54	10.40	1.96	21.45	5.31	23.21	8.74	12.06	3.56	20.64
Pinocchio <sup>+</sup>	5.50	9.11	3.20	19.75	5.20	20.40	1.60	9.31	3.70	24.38
Ours	0.77	6.81	0.56	8.62	3.96	14.12	0.60	4.92	1.47	13.70

Method	Swim		Jump		Walk3		Aggression		Howl	
	PMD	FVMD	PMD	FVMD	PMD	FVMD	PMD	FVMD	PMD	FVMD
NPR <sup>+</sup>	3.56	12.03	2.05	5.65	3.92	18.24	3.51	25.66	3.38	16.15
Transfer4D	5.21	12.31	3.11	8.19	3.39	7.60	4.87	31.32	4.26	7.00
Pinocchio <sup>+</sup>	4.80	7.83	16.30	6.71	10.30	17.73	6.60	25.63	7.90	14.00
Ours	2.23	7.61	1.66	2.71	0.75	4.94	1.26	18.72	1.05	6.11

Method	Hit Back		Run Stop		Run Forward		Drink		Hop Forward	
	PMD	FVMD	PMD	FVMD	PMD	FVMD	PMD	FVMD	PMD	FVMD
NPR <sup>+</sup>	2.25	10.02	5.61	12.39	4.74	5.02	2.80	27.67	2.55	23.48
Transfer4D	5.29	13.72	4.22	23.86	8.83	5.24	5.28	17.13	1.44	15.91
Pinocchio <sup>+</sup>	3.40	17.07	2.90	10.89	4.20	4.28	4.30	20.51	3.30	21.07
Ours	0.88	9.32	1.22	8.36	2.39	2.92	0.65	16.45	0.51	6.80

Table A9: **Quantitative evaluation across all scenes from the DT4D-others dataset.** PMD and FVMD values are reported in  $10^3$  and  $10^{-3}$  scales, respectively. Lower is better. Best and second-best results are highlighted in red and orange, respectively.

Method	Fly		Attack		Running		Walk		Swimming	
	PMD	FVMD	PMD	FVMD	PMD	FVMD	PMD	FVMD	PMD	FVMD
Transfer4D	13.21	45.51	2.67	21.40	14.08	11.15	3.59	3.80	2.25	5.74
Pinocchio <sup>+</sup>	2.91	30.63	2.14	11.01	29.99	17.37	0.43	8.97	2.45	3.18
Ours	1.56	36.07	1.81	9.71	5.19	11.26	0.57	3.36	0.62	4.63